JGR Atmospheres

RESEARCH ARTICLE

10.1029/2024JD041815

Key Points:

- Terrain slopes with and without upslope large roughness elements impact downslope stratification differently in the nighttime SBL
- Downslope airflow reduces downstream temperature not much stratification and downstream turbulence is enhanced by hydrostatic imbalance
- Cold air elevated by upslope large roughness reduces the downstream stratification and effectively enhances shear generation of turbulence

Correspondence to:

J. Sun,
jielun@nwra.com

Citation:

Sun, J., Bhimireddy, S. R., Kristovich, D. A. R., Wang, J., Hiscox, A. L., Mahrt, L., & Petty, G. W. (2025). Impacts of terrain slope and surface roughness variations on turbulence generation in the nighttime stable boundary layer. *Journal of Geophysical Research: Atmospheres*, *130*, e2024JD041815. https://doi.org/10.1029/2024JD041815

Received 17 JUN 2024
Accepted 20 JAN 2025

Impacts of Terrain Slope and Surface Roughness Variations on Turbulence Generation in the Nighttime Stable Boundary Layer

Jielun Sun[1], Sudheer R. Bhimireddy[2,3], David A. R. Kristovich[4], Junming Wang[4], April L. Hiscox[5], Larry Mahrt[1], and Grant W. Petty[6]

[1]NorthWest Research Associates, Boulder, CO, USA, [2]Cooperative Institute for Research in Environmental Sciences, University of Colorado, Boulder, CO, USA, [3]Global Systems Laboratory, National Oceanic and Atmospheric Administration (NOAA), Boulder, CO, USA, [4]Climate and Atmospheric Science Section, Division of State Water Survey, Prairie Research Institute, University of Illinois, Champaign, IL, USA, [5]Department of Geography, University of South Carolina, Columbia, SC, USA, [6]Atmospheric and Oceanic Sciences Department, University of Wisconsin-Madison, Madison, WI, USA

Abstract Terrain slopes with and without upslope large surface roughness impact downstream shear-generated turbulence differently in the nighttime stable boundary layer (SBL). These differences can be identified through variations in the relationship between turbulence and wind speed at a given height, known as the HOckey STick (HOST) transition, as compared to the HOST relationship over flat terrain. The transport of cold surface air from elevated uniform terrain reduces downstream air temperature not much air stratification. As terrain slope rises, the increasing cold and heavy air enhances downstream hydrostatic imbalance, resulting in increasing turbulence for a given wind speed. That is, the rate of turbulence increase with wind speed from downslope flow is independent of terrain slope. Upslope large surface roughness elements enhance vertical turbulent mixing, elevating cold surface air from the terrain. Horizontal transport of this elevated, cold, turbulent air layer reduces the downstream upper warm air temperature. Benefiting from the progressive reduction of downstream stable stratification with increasing height in the SBL, wind shear can effectively generate strong turbulence. In addition to the turbulence enhancement from the cold downslope flow, the rate of turbulence increase with wind speed is elevated. This study demonstrates key physical mechanisms for turbulence generation captured by the HOST relationship. It also highlights the influence of terrain features on these mechanisms through deviations from the HOST relationship over flat terrain.

Plain Language Summary This study investigates how terrain slope increase, with and without upslope large surface roughness such as trees and buildings, impacts downslope turbulence generation at night differently. The study demonstrates that the downslope air temperature decreasing with increasing terrain slope enhances downstream hydrostatic imbalance responsible for the vertical increase of turbulence. With the enhancement of turbulence from the hydrostatic imbalance, turbulence intensity for a given wind speed increases resulting in the observed shift of the near-neutral linear relationship between turbulence and wind speed toward increasing turbulence intensity. However, the rate of turbulence increase with wind speed is found independent of terrain slope variation. With an upslope tree patch on uniform terrain covered with corn stubble, the tree patch can enhance turbulent mixing such that the cold surface air over the upslope terrain is further elevated vertically. Horizontal transport of the elevated cold air layer can effectively reduce the downstream upper-level warm air temperature in the nighttime stable boundary layer. The vertical increasing reduction of the air temperature from the upslope tree patch results in effective generation of downstream turbulence by wind-shear. Consequently, the downstream turbulence increase with wind speed is enhanced with increasing height.

1. Introduction

Turbulence at a given height z over the flat and relatively homogeneous surface site of the Cooperative Atmosphere-Surface Exchange Study in 1999 (CASES-99) in the nighttime stable boundary layer (SBL) was observed to increase gradually and nonlinearly with mean wind speed V for weak winds and sharply and linearly with V when V exceeds its threshold value, V_s at z (Sun et al., 2012). The resulting relationship between turbulence and V resembles a hockey-stick as schematically illustrated in Figure 1. The intensity of turbulence in the hockey-stick relationship can be the square root of turbulence kinetic energy (TKE) V_{TKE}, or the standard

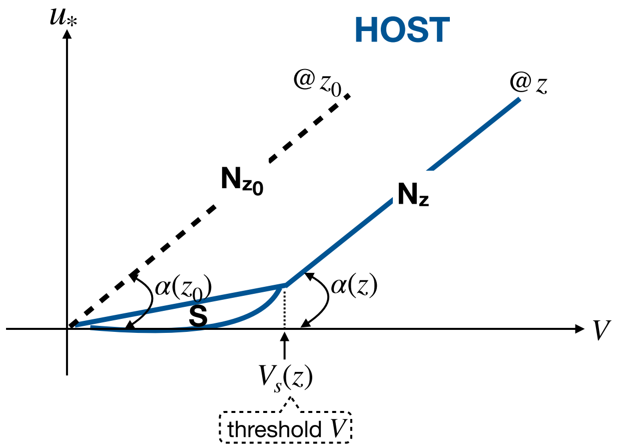

Figure 1. Schematic explanation of the observed HOST pattern (blue) between u_* and wind speed V at height z over a flat land surface with surface roughness length z_0 in the nighttime SBL. The blue linear line marked with N_z represents the near-neutral $u_* - V$ relationship at z; the area marked with S at the lower V end (enclosed by a short blue line and a blue curve) represents the stable regime at z. The two regimes are uniquely distinguished by the threshold wind speed $V_s(z)$. The black dashed line marked with N_{z0} represents the neutral $u_* - V$ relationship at z_0. The observed parallel between N_{z0} and N_z indicates that the neutral surface drag, $C_{dn} = [u_*(z_0)/V(z_0)]^2$ is uniquely determined by z_0, such that $\alpha(z) = \alpha(z_0)$. See the text for the physical processes reflected in the observed HOST pattern.

deviation of any wind component, or the square root of the vertical momentum flux $u_* = \sqrt{|\overline{w'V'}|}$ for a given surface roughness due to their direct connection with turbulence intensity. We use u_* to describe turbulence intensity in this study although turbulence intensity is sometimes defined as the standard deviation of wind speed over mean wind speed for an isothermal fluid (e.g., Stull, 1988).

The distinctive hockey-stick pattern as a function of V demonstrates the turbulence regime change in the SBL. Sun et al. (2016) indicated that the hockey-stick pattern reveals the importance of the bulk shear V/z as the largest wind shear at z instead of local wind shear $\partial V/\partial z$ for generation of the most energetic large turbulent eddies as well as the consequent reduction of the stable stratification by these eddies. Here the most energetic large turbulent eddies are defined as the eddies that contribute to the maximum perturbation of vertical wind. When V at z is weak at a given site, the most energetic large turbulent eddies generated by the weak V/z have the scale smaller than z. As a result, the cold air from the cooling surface remains near the surface under the relatively warm residual air from daytime, leading to the SBL. With increasing V, the stable stratification below z decreases due to turbulent transfer of cold air upward and warm air downward. Once V exceeds the threshold wind V_s at z, the increasing V/z is able to generate large turbulent eddies that scale with the vertical scale of the bulk shear, z, resulting in approximate elimination of the stable stratification below z. Further increasing V in the nearly neutral environment below z leads to a linear increase of u_* with V. Therefore, the stable and the nearly neutral or weakly stable turbulence regimes at z are separated by the critical bulk shear V_s/z and form a hockey-stick pattern. As z increases, the depth of the air layer between z and the surface increases, and the required bulk shear V_s/z for approximately eliminating the stable stratification below z increases, resulting in the systematic shift of the hockey-stick relationship toward increasing V. The parallel of the near-neutral linear relationship between u_* and V at different heights reflects the unique impact of the surface drag on turbulence generation under neutral conditions (more in Section 3.2). After extending the investigation of the relationship between turbulence intensity and wind speed to unstable conditions, Sun et al. (2016) named the hockey-stick pattern as the HOckey STick (HOST) transition.

In brief, the observed HOST pattern reflects two important physical processes in the SBL: bulk shear, V/z, for its critical contribution to mechanical turbulence generation and the consequent reduction of the atmospheric stratification by shear-generated turbulent mixing. In the atmospheric boundary layer (ABL), the atmospheric stratification is, without any significant weather event, strongly controlled by thermal energy transfer from surface heating/cooling through turbulent mixing. Thermally generated turbulence relies on unstable atmospheric stratification and cannot eliminate the unstable stratification to reach a neutral state. Conversely, mechanically generated turbulence depends on bulk wind shear, V/z, where any change of mean wind speed V is mainly controlled by the synoptic/mesoscale horizontal pressure gradient based on the horizontal momentum balance. Because the synoptic/mesoscale horizontal pressure gradient is approximately independent of the local atmospheric stratification, bulk-shear generated turbulence not only contributes to turbulence intensity but also reduces atmospheric stratification at the same time.

Because the HOST $u_* - V$ relationship essentially captures the critical factor of the bulk shear in turbulence generation and stratification variation in the surface layer, unsurprisingly, numerous studies have identified the HOST pattern over a variety of surfaces. The HOST pattern has been observed over sea surfaces (e.g., Andreas et al., 2012; Cheng et al., 2023; Sun & French, 2016), over open pasture (e.g., van de Wiel et al., 2012), within forests (e.g., Peltola et al., 2021; Russell et al., 2016), over Amazon forests (e.g., Dias-Júnior et al., 2017; Mendonça et al., 2023), over snow/ice on the Antarctica plateau (e.g., Mazzola et al., 2021; Vignon et al., 2017), over urban canopies (e.g., Huang et al., 2017; Liang et al., 2018), over complex terrain (e.g., Acevedo et al., 2015), and over coastline under the influence of typhoon strong winds (e.g., Lan et al., 2023). The well-known nighttime turbulence intermittency has been observed as the temporal variation of turbulence intensity jumping between stable and near neutral regimes in response to wind speed oscillations (e.g., Barbano et al., 2022; Cava et al., 2015; Mortarini et al., 2018; Román-Cascón et al., 2015; Sun, Mahrt, et al., 2015; Sun, Nappo, et al., 2015). Recently, Acevedo et al. (2021) and Shao et al. (2023) have investigated what controls the threshold wind speed for the regime transition. The contrast between the HOST observation and the MOST formulation was also theoretically investigated by Grisogono et al. (2020).

Sun et al. (2020) further elaborated the physical processes revealed by the observed HOST pattern, contrasted these with the implications of Monin-Obukhov Similarity Theory (MOST), and highlighted similarities and differences between MOST and observations. The observed HOST pattern at a given z reflects the contribution of large turbulent eddies in response to V/z to u_* in the stratified, stable or unstable surface layer. This important physical aspect of turbulence generation and impacts of the most energetic large turbulent eddies on the atmospheric stratification demonstrated in the observed HOST is not reflected in the MOST mathematical approach for formulating turbulence similarity relationships. As z approaches to the surface, such as less than 1 m, the difference between local shear $\partial V/\partial z$ and bulk shear V/z becomes negligible, and MOST has been observed to approximately reflect field observations. With decreasing z, the corresponding V_s approaches to zero as illustrated in Figure 1; the thin surface layer below z is approximately neutral all the time.

Obviously, without a range of wind speed variation, the characteristic HOST pattern for the turbulent regime transition between non-neutral and near neutral regimes would not be observed (Sun et al., 2020). Failure to establish the nocturnal stable stratification can be due to either lack of effective surface cooling, such as under dense clouds or reduced surface exposure from surrounding environment (e.g., Hoch et al., 2011; Lehner et al., 2015; Maillard et al., 2022; Noad & Bonnaventure, 2024; Pfister et al., 2019; Wang et al., 2022), or lack of the effective warming of the residual layer from the daytime convective heating before sunset such as on a raining day (Sun et al., 2020). Persistent strong winds for V much larger than V_s at night can also prevent the formation of the stable layer at night. Without significant stable or unstable stratification, the HOST $u_* - V$ relationship at a given height is dominated by the near neutral regime only.

The HOST pattern observed over the flat CASES-99 surface in the clear nighttime SBL provides a guidance for the relationship between u_* and bulk wind shear for the turbulence regime transition when turbulence variation is only impacted by bulk wind shear and stable stratification. Additional physical mechanisms beyond bulk wind shear, such as significant surface roughness changes and terrain slope variations in complex terrain, can also impact turbulence intensity (e.g., Bhimireddy et al., 2024; Mahrt et al., 2015; Mahrt et al., 2018; Mahrt & Heald, 2015; Medeiros & Fitzjarrald, 2015). These additional environmental influences can be investigated by comparing an observed HOST in complex terrain with a reference HOST pattern over a uniform flat surface.

Following previously observed HOST relationships, we extend the investigation of shallow complex terrain by Bhimireddy et al. (2024). Based on our systematic investigation of the observed $u_* - V$ relationship from shallow complex terrain at clear nights, we identify that terrain slope increase with and without upslope large surface roughness elements contribute differently to the deviation of the observed downstream $u_* - V$ relationship from its corresponding relationship over relatively flat terrain in the same observation domain (the first part of Section 3). By conducting theoretical and field data analyses, we investigate physical processes responsible for the observed deviations (the second part of Section 3). Two field campaigns in shallow complex terrain are used in this study (Section 2). The main results and conclusions are summarized in Section 4.

2. Field Observations and Data Analysis

2.1. SAVANT

The Stable Atmospheric Variability and Transport (SAVANT) field campaign took place in an agricultural field of corn and soybean in shallow complex terrain, north of Mahomet, Illinois, during September–November 2018 (Bhimireddy et al., 2022, 2024; Hiscox et al., 2023). The field was harvested on 14–16 October, 2018. We only concentrate on the post harvest period after 16 October, 2018. In general, the shallow complex terrain elevation decreases eastward (Figure 2a). The elevation map in Figure 2a is based on a high-resolution geographically registered digital elevation model (DEM) derived from a dense array of overlapping images of the SAVANT field site taken from a fixed wing unmanned aerial system (Petty, 2019). A main gully with two gentle hills on two sides is about 10-m wide and covered with short grass; the south hill is about 5 m higher than the north one within 200 m from the main gully. The eastward descending main gully turns southeast at the east end and is joined by

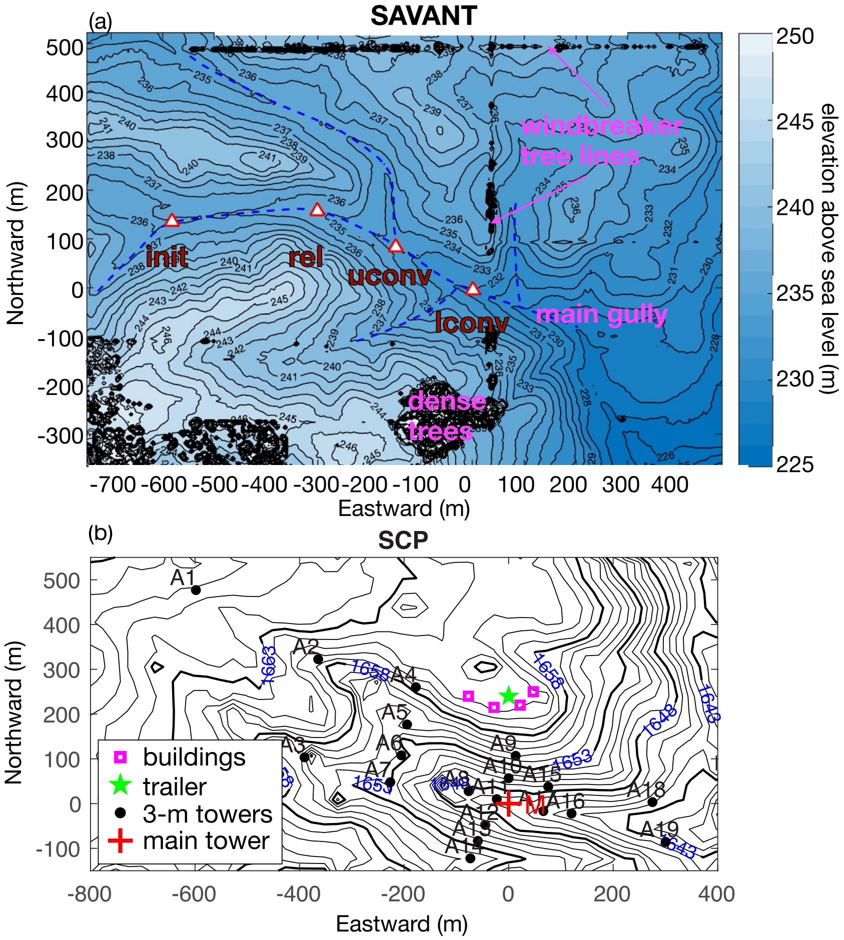

Figure 2. The SAVANT (a) and the SCP (b) elevation maps in m above sea level. In (a), the four towers– init, rel, uconv, and lconv are marked with red triangles along the eastward descending main gully jointed by three small gullies on both sides, where all the gullys are marked with blue dashed curves. Tree patches and wind-breaker tree lines are reflected in densely packed black contour lines, where the average tree height of the dense tree patch south of lconv is about 22 m, and the average tree height of the windbreaker tree line is about 28 m. In (b), observations used in this study are from the 20-m main tower marked with red plus and letter M; the structures on the north plateau that impact the observation are also marked. Investigation of observations from 19 3-m towers marked with A1 to A19 can be found in Mahrt et al. (2014).

two small gullies from the north and south sides at the east end. The heavily wooded areas with trees are marked with dense black contour lines.

Four towers were instrumented along the main gully. From west to east, there are “initiation” (Init), “release” (rel), “upper convergence” (uconv), and “lower convergence” (lconv) towers at 236, 235.5, 233.5, and 232 m above sea level (ASL) (Figure 2a). That is, the terrain elevation change between the top and the bottom tower along the main gully is about 4 m. Three-dimensional CSAT3 sonic anemometers were installed at 1.5, 3, 4.5, 6, 8.5, 10, 15, and 20 m above the ground on the 20-m rel and lconv towers and at 1.5, 3, 4.5, 6, and 10 m on the 10-m init and uconv towers (NCAR/EOL In-situ Sensing Facility, 2021). All the sonic anemometer measurements were sampled at 20 s^{-1}. Sensiron SHT75 humidity and temperature sensors in aspirated shields were installed at 0.2, 1.5, 4.5, and 10 m on the two 10-m towers and at 0.2, 1.5, 4.5, 8.5, 15, and 20 m on the two 20-m towers with the sampling rate of 1 s^{-1}. On the rel and lconv towers, Hukseflux NR01 integrated 4-component radiometers were installed at 20 m, Campbell EC150 H_2O/CO_2 analyzers with the sampling rate of 20 s^{-1} and Vaisala PTB110 analog barometers with the sampling rate of 1 s^{-1} (internal to the Campbell EC150 H_2O/CO_2 analyzers) were installed at 1.5, 6, and 20 m, and Paroscientific-6000 nanobarometers with the sampling rate of 10 s^{-1} were installed at 1.5 and 20 m. On the init and uconv towers, Campbell EC150 H_2O/CO_2 analyzers and solid-state barometers (internal to the Campbell EC150 H_2O/CO_2 analyzers) were installed at 1.5 and 6 m.

2.2. SCP

The Shallow Cold Pool Experiment (SCP) was conducted over semiarid grasslands in northeast Colorado from 1 October to 1 December 2012 (Mahrt, 2017, 2022; Mahrt et al., 2014; Mahrt & Heald, 2015). The main valley is, on average, about 12 m deep and 270 m long (Figure 2b). We focus on observations from eight Campbell Scientific three-dimensional CSAT3 sonic anemometers at 0.5, 1, 2, 3, 4, 5, 10, and 20 m sampled at 20 s^{-1} on the main tower in the valley (marked M in Figure 2b) and the 5-min averaged downward solar and longwave radiation measurements at 1.5 m above the surface at tower A11 about 20 m from the M tower (UCAR/NCAR—Earth Observing Laboratory, 2014).

2.3. Data Analysis

To address airflows in complex terrain, we use the standard Cartesian coordinate system with the vertical direction in parallel with gravity due to its unique role in the vertical distribution of air density and the vertical stratification. Thus, the words "downward" used in this study refers to the direction of gravity.

Turbulence intensity in this study is expressed as $u_* = \left(\overline{w'u'}^2 + \overline{w'v'}^2\right)^{1/4}$ at all observation heights, where w is the vertical velocity, $\overline{w'u'}$ and $\overline{w'v'}$ are momentum fluxes in the zonal and meridional directions, and the prime represents turbulence perturbations from Reynolds averaged means expressed with the overline. Because the most energetic turbulent eddies scale with height (e.g., Sun et al., 2016, 2020; Wyngaard, 2010), and the highest observation level is 20 m above the ground in both field campaigns, 5-min data segments include the most energetic turbulent eddies at all tower heights. The 5-min averaged mean and turbulence variables such as u_* are used for both field data analyses in this study. Sonic anemometer observations were corrected for their orientation measured by Leica Geosystem and through the standard tilt correction used by the National Science Foundation (NSF)/National Center for Atmospheric Research (NCAR)/Earth Observation Laboratory (EOL) (NCAR/EOL In-situ Sensing Facility, 2021).

Two types of pressure sensors–Paroscientific nanobarometers and Vaisala PTB110 analog barometers were used for SAVANT. Comparison between the two colocated at 1.5 and 20 m on the rel tower indicates that the difference between the two sensors is approximately constant and the standard deviation between them during the entire field campaign is about 0.1 mb. Thus, we consider 0.1 mb as the uncertainty value for pressure measurements.

Clouds appeared frequently during both 2-months field campaigns (Hiscox et al., 2023; Pfister et al., 2019). To avoid the influence of clouds on the SBL development (Sun et al., 2020), we identify clear nights by examining the downward solar radiation variation before each night and the downward longwave radiation variation during the night to ensure potential nighttime stable stratification without any significant cloud influence. For SAVANT, 10 clear nights are selected: 20, 21, 24–27 October and 1, 13, and 25–26 November. For SCP, 33 clear nights are selected: 22, 23, 29 September, 4, 8, 9, 12,15–19, 22–24, 31 October, and 1, 3, 4, 6–10, 12,14 16, 18, 19, 21–23, 28 November.

3. Impacts of Terrain Slope Increase With and Without Upslope Large Surface Roughness Elements on Downstream Turbulence Generation

The nighttime SBL is developed through thermal diffusion across the longwave radiatively-cooled ground surface in the relatively thin surface laminar layer and the upward transfer of the cold air by turbulent mixing above the laminar layer into the relatively warm residual air from daytime surface heating (e.g., Geiger et al., 1995). Due to the limited distance of molecular movement in thermal diffusion, the SBL is strongly controlled by turbulent mixing generated by bulk shear. We find that the $u_* - V$ relationship from all the towers for wind from the northwest (NW) sector at the SAVANT site (Figure 3) shows the consistent HOST pattern as observed at the relatively flat CASES-99 site (Sun et al., 2012). This is because the wind from the NW sector is mainly from the west-northwest (WNW) direction (marked by the black arrow in Figure 3a) with relatively small terrain variations for all the towers and the observed wind speed ranges from near 0–10 m s^{-1}, which covers both stable and near neutral regimes. Because the surface cover of corn stubble from this wind sector represents the dominant surface type at the site during the period of this study, we use the HOST pattern from the NW sector as the reference HOST for the SAVANT site to investigate impacts of the shallow complex terrain on turbulence variation.

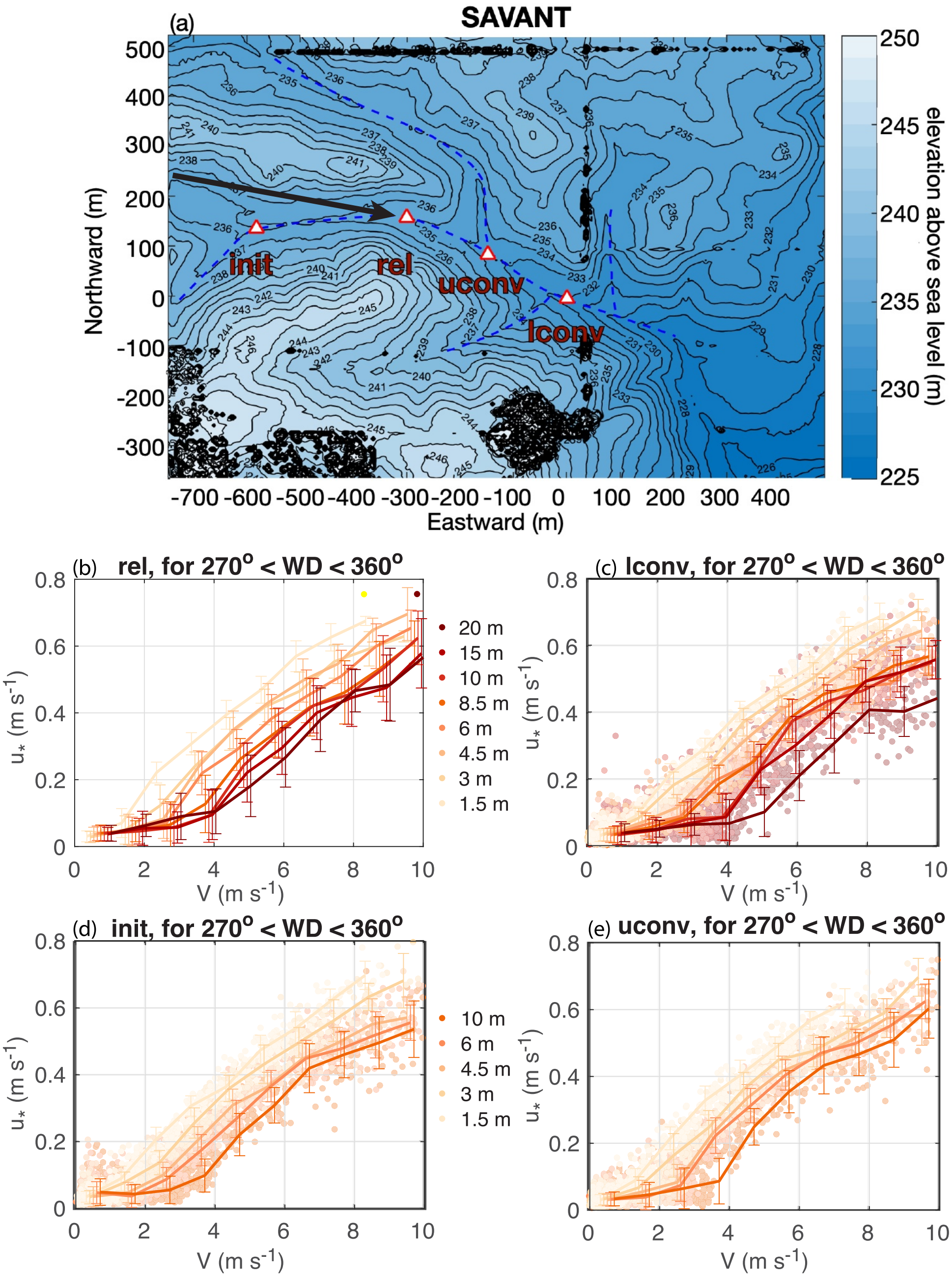

Figure 3. The HOST $u_* - V$ relationship at all the observation heights on the four towers for the wind direction (WD) between 270° and 360° during SAVANT. Each dot represents 5-min averaged data at the observation height represented by the color of the height. The thick curves represent the bin-averages of $u_* - V$ at different heights. The vertical thin bars along each bin-averaged $u_* - V$ curve represent the standard deviations of u_* from each wind speed bin. To make the bin-averaged curves visible, the transparency of all the dots is reduced. The wind direction in this wind sector is dominated by the wind direction marked with the black arrow in (a) over the dominant corn stubble surface during the post harvest period, from which the terrain elevation variation is negligible.

We then systematically examine the $u_* - V$ relationship at 1.5, 4.5, and 10 m from all the four towers and additional levels at 15 and 20 m from the two 20-m towers for all the coming wind-direction sectors at every 45° except the north–northeast sector from which the observation for the selected clear nights is limited (Figure 4). We find striking differences among all the observed near-neutral $u_* - V$ relationships in comparison with the

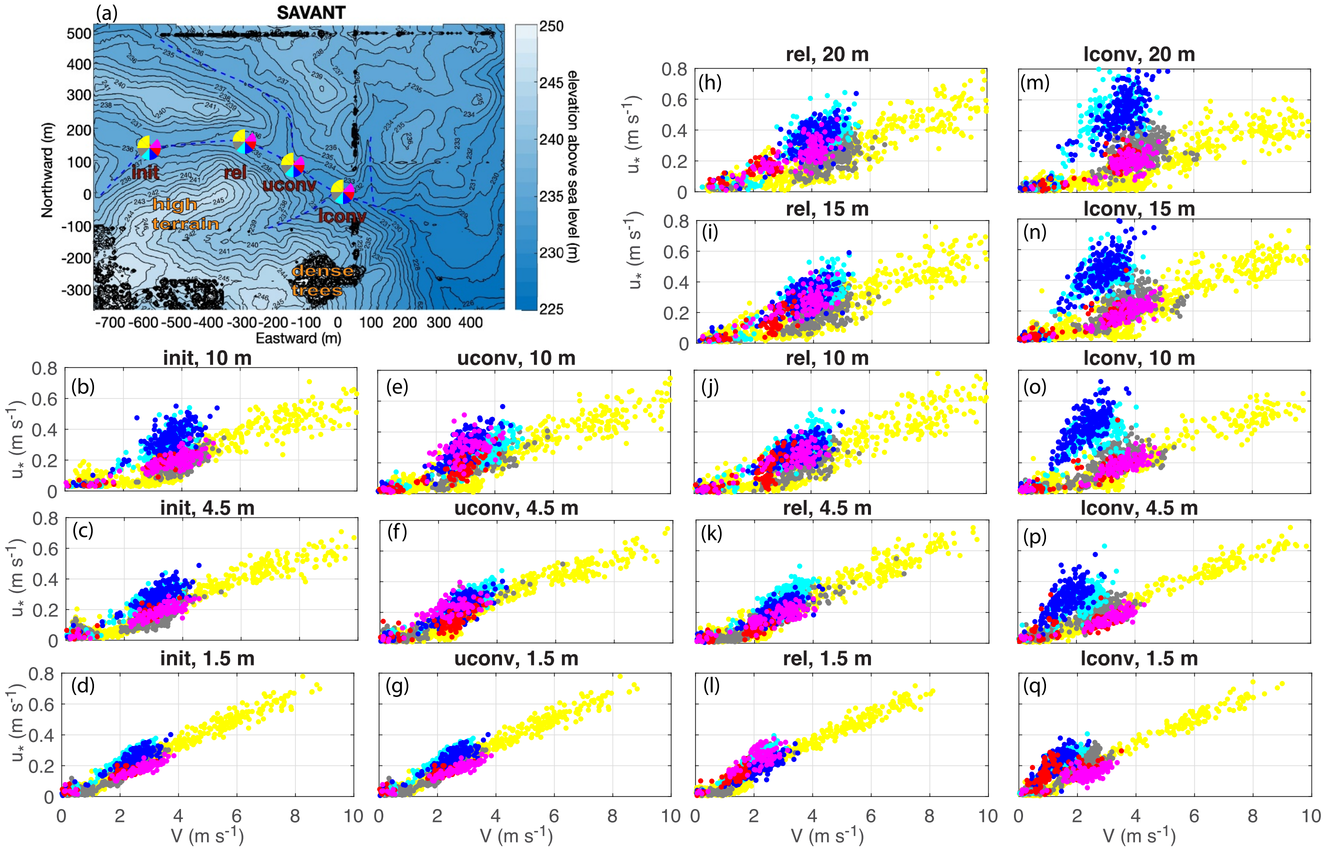

Figure 4. The observed $u_* - V$ relationship at the observation height marked at the top of each panel for the init (b–d), the uconv (e–g), the rel (h–l), and the lconv (m–q) towers, where the colors of the dots correspond to the colors of the wind sectors marked in (a). The light yellow dots in each panel represent the reference HOST at the same observation height over the relatively flat terrain as shown in Figure 3.

reference HOST for wind from the NW sector observed at the same locations. The near-neutral u_* increase with V significantly higher than the reference one is found at the lconv tower for wind from the patch of dense trees with the average tree height of 22 m on the hill south of the lconv tower (cyan wind sector in Figure 4a) and from a patch of the north–south oriented windbreaker tree line southeast of lconv with the average tree height of about 28 m (blue wind sector in Figure 4a). The enhancement of the u_* increase with V is observed to decrease with increasing distance between towers and the upslope tree patch south of lconv as shown in the difference between the uconv and the lconv towers at 10 m. Evidently, the upslope large surface roughness of the tree patch on the sloping terrain covered with the small surface roughness of corn stubble enhances the u_* increase with V, and the impact fades away as the distance between the upslope tree patch and the downstream observation tower increases. The dense tree patch does not seem to impact the enhancement of the u_* increase with V if the observation height is below the elevation of the tree patch base such as at 1.5 and 4.5 m on the uconv and rel towers downslope of the tree patch. Furthermore, we find the parallel shift of the near-neutral $u_* - V$ relationship toward large u_* from the corresponding reference HOST for wind directions from the large hill south of the main gully (marked as “high terrain” in Figure 4a), such as at the init and rel towers.

From the systematic examination of the observed $u_* - V$ relationships as functions of observation height and wind direction at all the SAVANT towers, we find terrain slope increase with or without upslope large surface roughness elements impacts the deviation of the observed near-neutral $u_* - V$ relationship from the reference HOST differently. We first investigate terrain slope variation alone on downstream turbulence generation in Section 3.1. We then study how a sloping terrain with additional upslope large surface roughness elements impact downstream turbulence generation differently in Section 3.2.

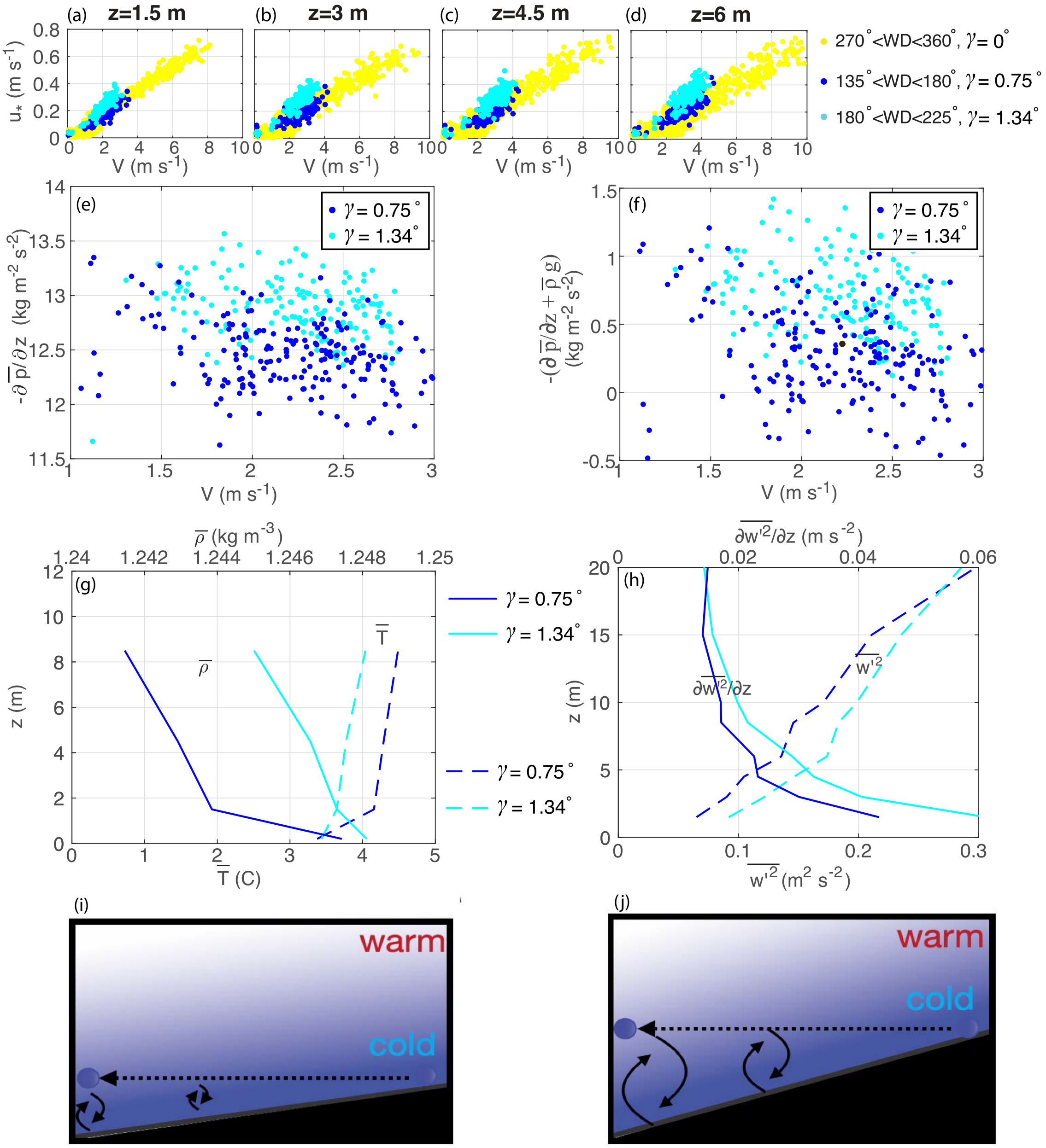

Figure 5. The observed parallel shift of the near-neutral $u_* - V$ relationship toward increasing u_* with increasing terrain slope γ at the rel tower in (a–d) can be explained by the contribution of the downslope increasing cold air [dashed curves in (g)] to the enhancement of $-\partial\overline{p}/\partial z$ (e), air density $\overline{\rho}$ [solid curves in (g)], and hydrostatic imbalance, $-(\partial\overline{p}/\partial z + \overline{\rho}g)$ (f) for increasing $\partial\overline{w'^2}/\partial z$ [solid curves in (h)] and $\overline{w'^2}$ [dashed curves in (h)] for the two terrain slopes of $\gamma = 0.75°$ and $1.34°$. The decreasing air temperature with increasing terrain slope due to the vertical turbulent mixing of the horizontal transport of the cold surface air from an elevated terrain is schematically illustrated in (i, j), where the shade of the blue color represents the vertical temperature variation in the SBL.

3.1. Impacts of Terrain Slope Variation Alone on Downstream Turbulence Generation

We investigate how terrain slope change with a uniform terrain surface impacts downstream turbulence generation in comparison with the reference HOST at the rel tower for its 20-m height with more levels of measurements than the others and its close proximity to the highest ridge in the observation domain. We choose two wind sectors with two terrain-slopes (γ) and the same surface roughness of corn stubble for this investigation: wind from the south-southwest (SSW) direction of 180–225° down from the relatively steep slope of $\gamma = 1.34°$ (cyan in Figures 5a–5d) and wind from the south-southeast (SSE) direction of 135–180° down from the relatively gentle slope of $\gamma = 0.75°$ (blue in Figures 5a–5d). Because the observed signal of the impact of the dense tree patch on the observed $u_* - V$ relationship becomes negligible when the elevation of the observation is below the elevation of the tree-patch base, we analyze observations from the bottom four levels on the rel tower for wind from the SSE direction, which are impacted by the sloping terrain from the SSE direction only. Figures 5a–5d show that γ enhances u_* for a given V larger than $V_s \approx 2$ m s^{-1}, resulting in the systematic shift of the near-neutral $u_* - V$ line.

To investigate the near-neutral $u_* - V$ relationship, we first examine the balance equation for vertical momentum fluxes along wind direction, $\overline{w'V'}$. Because a terrain slope can impact turbulence generation vertically and horizontally depending on the horizontal and vertical distances between the observation point and the terrain surface, we estimate the ratio between the two distances. For a hill with the slope angle γ, the horizontal distance from a point at height z in parallel to the gravity above the sloping surface to the uphill terrain surface is $x = z \arctan(\gamma)$. The smallest ratio of x/z among the three terrain slopes in Figures 5a–5d is about 43 from the relatively steep SSW slope. The significantly large horizontal distance x to the upstream terrain surface relative to the vertical distance z indicates that $\overline{w'V'}$ at z is strongly influenced by the surface drag due to interactions between airflows and the surface below. With a uniform surface roughness, the horizontal variation of $\overline{w'V'}$ would be negligibly small. Knowing that the averaged w over many up and down turbulent vertical motions, $\overline{w}$, is much smaller than the amplitude of vertical turbulent motions (e.g., Sun et al., 2024), the Reynolds-averaged equation for $\overline{w'V'}$ can be approximated as (e.g., Garratt, 1992)

$$\frac{\partial \overline{w'V'}}{\partial t} \approx -\overline{w'^2}\frac{\partial V}{\partial z} + \frac{\overline{w'\rho'}}{\overline{\rho}^2}\frac{\partial \overline{p}}{\partial x} + f_\mu, \tag{1}$$

where ρ and p represent air density and pressure, respectively, and the overline for V in the first term on the righthand side (RHS) is omitted here for simplicity and consistency with V used in the study. The last term on the RHS of Equation 1 is the impact of dynamic air viscosity μ as a result of airflow deformation on $\partial\overline{w'V'}/\partial t$ and is normally small away from the surface. The term $\partial\overline{p}/\partial x$ in the second term on the RHS represents the mesoscale-synoptic scale horizontal pressure gradient responsible for the acceleration of mesoscale-synoptic horizontal wind. Under near neutral conditions, the vertical turbulent heat flux is negligibly small. Because air density variation is strongly controlled by air temperature variation through thermal expansion/contraction (e.g., Sun et al., 2024), the negligibly small vertical air density flux under near neutral conditions results in the negligibly small second term on the RHS in comparison with the first term. As the wind direction variation in the near-neutral regime is relatively small (e.g., Sun, Mahrt, et al., 2015), the difference between $-\overline{w'V'}$ ($\overline{w'V'}$ is negative near the surface) and $\left(\overline{w'u'}^2 + \overline{w'v'}^2\right)^{1/2}$ is approximately less than 5% under strong wind conditions. Applying $u_*^2 \approx -\overline{w'V'}$ and integrating Equation 1 over a given small time interval Δt, we have

$$u_*^2 \approx \overline{w'^2}\frac{\partial V}{\partial z}\Delta t. \tag{2}$$

Because of the dominance of the bulk shear V/z for $\partial V/\partial z$, the near-neutral u_*^2 for a given V at a given z from different terrain slopes would be directly related to their $\overline{w'^2}$ values.

We then examine the variation of $\overline{w'^2}$ using the equation for vertical motions. Based on the discussion for obtaining Equation 2, the Reynolds averaged equation for vertical motions can be approximated as (e.g., Sun et al., 2024)

$$\overline{\rho}\frac{\partial\overline{w'^2}}{\partial z} \approx -\left(\frac{\partial\overline{p}}{\partial z} + \overline{\rho}g\right). \tag{3}$$

Sun et al. (2024) found that the hydrostatic imbalance, $-(\partial\overline{p}/\partial z + \overline{\rho}g) \neq 0$ contributes directly to the vertical variation of $\overline{w'^2}$ based on their analyses of field observations from towers, Doppler lidar and radar, and global positioning system (GPS) soundings. They validated that $-(\partial\overline{p}/\partial z + \overline{\rho}g) > 0$ is responsible for the vertical increase of $\overline{w'^2}$ from its surface zero value.

We then investigate whether $\overline{w'^2}$ increases with the terrain slope as a result of hydrostatic imbalance. To avoid the significant influence of the dense tree patch south of lconv on turbulence observation at the rel tower explained above, we use the PTB110 air pressure measurements at 1.5 and 6 m to calculate the magnitude of the vertical pressure gradient, $-\partial\overline{p}/\partial z > 0$ (the atmospheric pressure decreases with height). We find that the vertical variation of air pressure between the two levels is larger than the pressure uncertainty value of 0.1 mb (Section 2.1), indicating that the measured vertical pressure difference is beyond the instrument uncertainty. For a given $V > V_s$, $-\partial\overline{p}/\partial z$ is observed to increase with terrain slope γ (Figure 5e).

To investigate the impact of the air density variation on hydrostatic imbalance, we study the vertical temperature profiles from the two slopes as air density is strongly controlled by thermal expansion/contraction. We find that the wind-sector averaged air temperatures from the two terrain slopes are similar at 0.2 m as the air temperature adjacent to the surface is uniquely influenced by the local land surface temperature. With increasing height above 0.2 m, the air is colder from the relatively steep slope than from the gentle slope with no significant stratification change between the two directions (dashed curves in Figure 5g). As the air temperature increases with height in the SBL, the colder air from the steep slope reduces the vertical temperature increase from 0.2 to 1.5 m. The colder air from the steep slope can be explained schematically by comparing Figure 5i for a gentle slope with Figure 5j for a steep slope. As the cold surface air from a point on a sloping terrain is transported downstream by horizontal wind in response to the horizontal pressure gradient at the location, the most energetic large turbulence generated by the bulk shear V/z at any point downstream would vertically mix the cold upslope air into the air layer below under near-neutral conditions. Because the air temperature increases with height in the weakly SBL, the air temperature contrast between the upslope cold surface air and the downstream air at the same elevation would increase with the terrain slope as shown in the color contrast between the blue dot from the upslope surface and the surrounding color downstream in Figures 5i and 5j. That is, more cold surface air along the terrain slope would be entrained into the downstream air column from steep terrain than shallow terrain through the vertical turbulent mixing generated by local bulk shear along the terrain slope. Therefore, the vertical mixing of the upslope cold air would result in decreasing downstream air temperature with increasing terrain slope as observed in Figure 5g.

Using the air density calculated from the ideal gas law with measured water-vapor specific humidity, air temperature, and air pressure, we find that air density $\overline{\rho}$, on average, increases with decreasing air temperature as a result of thermal contraction (solid curves in Figure 5g), resulting in the air density increase with terrain slope. Because air pressure is strongly influenced by the column air mass weight above, the increasing air density in the air layer impacted by the transport of the cold air from elevated terrain would enhance the downslope vertical air pressure gradient, which is indeed observed in Figure 5e.

Applying the observed $-\partial\overline{p}/\partial z$ and $\overline{\rho}$, $-(\partial\overline{p}/\partial z + \overline{\rho}g)$ is larger for the steep slope than for the gentle slope (Figure 5f). This result is consistent with the observation in Sun et al. (2024) due to the dominance of the positive $-\partial\overline{p}/\partial z$ in $-(\partial\overline{p}/\partial z + \overline{\rho}g)$ even though the increasing air density by itself reduces the hydrostatic imbalance through $-\overline{\rho}g$. Thus, $\partial\overline{w'^2}/\partial z$ (solid curves in Figure 5h) in response to the observed $-(\partial\overline{p}/\partial z + \overline{\rho}g)$ is larger for the steep slope than for the gentle slope as implied in Equation 3. Therefore, $\overline{w'^2}$ (dashed curves in Figure 5h) from its zero surface value is larger for the steep slope than for the gentle slope. Consequently, for a given V, u_* is larger for the steeper slope (Equation 2), and the near-neutral $u_* - V$ linear relationship from downslope wind shifts toward large u_* in parallel with the reference $u_* - V$ line over the relatively flat terrain as observed in Figures 5a–5d.

3.2. Impacts of Sloping Terrain With Upslope Surface Roughness on Downstream Turbulence Generation

The impact of surface roughness variations on the $u_* - V$ relationship has been observed, for example, by Mahrt et al. (2013) and Sun and French (2016) over relatively flat surfaces and by Bhimireddy et al. (2024) over complex terrain. Because the surface drag coefficient under neutral conditions $C_{dn} = [u_*(z_0)/V(z_0)]^2$ over a flat terrain is invariant for a given z_0, once the stable stratification in the air layer below z is reduced to near neutral by energetic large turbulent eddies that scale with z, the turbulent mixing at z over the same surface is impacted by the same C_{dn}. Therefore, the u_* increase with V under near-neutral conditions at any z remains the same with increasing z (Figure 3). Note that the surface roughness z_0 reflects the net dynamic impact of surface roughness elements on the surface turbulent momentum flux and is not necessarily related to the physical height of surface roughness

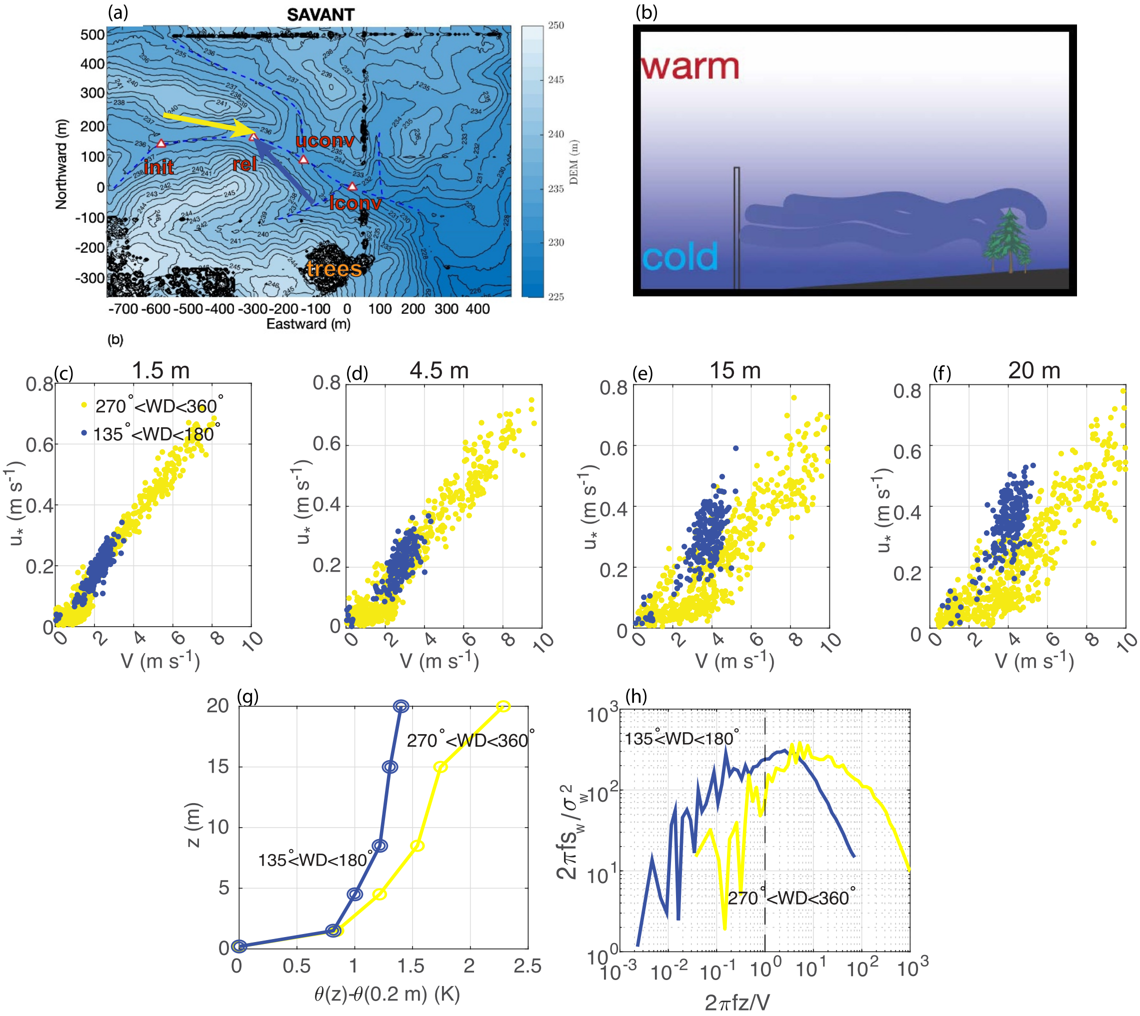

Figure 6. Comparison between the $u_* - V$ relationships for wind direction (WD) from the upslope tree patch direction, $135 - 180°$ [blue dots in (c–f) corresponding to the blue wind vector in (a)] and from the reference WNW sector, $270 - 360°$ [yellow dots in (c–f) corresponding to the yellow wind vector in (a)]. Comparison of the mean stable stratification in (g) is shown as the averaged potential temperature profiles relative to their surface values at 0.2 m for $V > 2$ m s^{-1} at 15 m from the two directions. Comparison of the normalized w power spectra S_w, $2\pi f S_w/\sigma_w^2$ as a function of the normalized frequency f, $2\pi fz/V$, at $z = 10$ m for the two wind directions is demonstrated in (h), where σ_w is the standard deviation of w. To ensure the similar wind speeds for the comparison in (h), the sonic anemometer measurements between 0000 and 0100 CST on 24 October for the WNW wind and on 26 November for wind from the tree patch with $V \sim 5$ m s^{-1} at $z = 10$ m from both wind directions are used; the black dashed line represents $2\pi fz/V = 1$. The impact of the cold turbulent airflow generated by the upslope large tree-patch on the increasing reduction of the downstream stable stratification is schematically illustrated in (b), where the blue shade represents the air temperature variation as in Figures 5i and 5j.

elements. Because the neutral u_* increase with V is related to C_{dn} and C_{dn} increases with z_0, the u_* increase with V is enhanced with increasing z_0.

3.2.1. SAVANT

Here we investigate the contribution of the dense tree patch up the SSE terrain slope to the near-neutral $u_* - V$ relationship at the rel tower for its vertical coverage and its direct line of sight of the tree patch (Figure 6). Examining Figure 6c indicates that near the surface such as at 1.5 m, the $u_* - V$ relationship is independent of terrain slope indicating that the local bulk shear near the surface over the same local z_0 plays a dominant role in generating turbulent mixing. As z increases to the elevation above the base of the tree patch, such as at 15 and 20 m (Figures 6e and 6f), the influence of the downslope cold air on u_* discussed in Section 3.1 is seen in the relatively larger u_* in comparison with the reference one at the threshold wind $V_s \approx 4$ m s^{-1} when u_* just reaches to its near-neutral value. With increasing V in the near-neutral regime, the relatively large u_* increase with V in comparison with the reference $u_* - V$ relationship is observed. Because z_0 associated with the dense tree patch is larger than z_0 associated with corn stubble, and the terrain slope does not contribute to the u_* increase with V (Section 3.1), the observed large u_* increase with V from the upslope tree patch direction in comparison with the one from the reference wind sector over corn stubble in Figures 6c–6f may seem to be consistent with the above discussion on the impact of z_0 on the increase u_* with V. Interestingly, the enhancement of the u_* increase with V is observed to increase with height instead of being invariant as in the reference HOST over the flat surface. Therefore, the observed near-neutral $u_* - V$ relationship for wind from the upslope tree patch is beyond the simple added impacts of the individual terrain features of large z_0 and the terrain slope.

By comparing the averaged potential temperature profiles at the rel tower for wind from the SSE sector in the direction of the tree patch and from the reference WNW sector, we find that the upslope tree patch results in the increasing reduction of the downstream stable stratification with height such that the stratification is stable below the elevation of the tree-patch base about 6.5 m at the rel tower and nearly neutral above instead of becoming increasingly stable with height as for wind from the reference sector (Figure 6g). The increasing reduction of the stable stratification with height can be explained by the enhanced turbulent mixing over the upslope tree patch as schematically illustrated in Figure 6b. Because of the enhanced turbulent mixing around the large surface roughness of the tree patch for a given V, the cold surface air is transported higher around the tree patch than over corn stubble downslope. The horizontal transport of this relatively deep cold turbulent air layer into the downstream upper warm air results in the significant reduction of the downstream stable stratification with increasing height. Therefore, the influence of the upslope tree-patch on the downstream stratification is significantly different from the upslope terrain alone based on the comparison between Figures 5g and 6g.

We further investigate w power spectra at rel for V around 5 m s^{-1} at 10 m from both directions as turbulence intensity at a given location is dominated by the most energetic large turbulent eddies generated by local bulk shear with the maximum turbulence perturbation at the peak of the w power spectrum, S_w (e.g., Sun et al., 2020). Comparison between the normalized S_w for V from the two directions indicates that the stable stratification reduction due to the upslope tree patch helps the bulk shear to effectively generate stronger turbulence with larger turbulent eddies as shown in the shift of its normalized S_w peak toward low frequency, f, normalized by V/z (Figure 6h). As the S_w peak at $2\pi fz/V = 1$ represents the scale of the most energetic turbulent eddies is z (e.g., Sun et al., 2020), the observed $2\pi fz/V < 1$ for wind from the upslope tree-patch indicates that the most energetic large turbulent eddies generated by the bulk shear for wind from the upslope tree-patch is not large enough to eliminate the stable stratification in the air layer below, which is evident in its temperature profile in Figure 6g. Because the nearly neutral layer in the upper rel for wind from the tree patch, the difference between the stable stratification below 15 and 20 m is relatively small, the u_* increase with V is not significant between 15 and 20 m.

Considering energy dissipation of the relatively strong turbulence around the upslope tree patch during the airflow traveling from the tree patch to the rel tower and the relatively weak turbulent mixing generated by bulk shear along the airflow over the sloping terrain covered with corn stubble, the observed vertical enhancement of the u_* increase with V cannot be explained by the advection of the enhanced turbulence over the tree patch. When the relatively strong turbulent airflow travels from the upslope tree patch to the rel tower over the distance of ∼500 m, turbulence energy dissipation would reduce u_*. In consideration of the airflow in generating turbulence through bulk shear along its path over the sloping terrain, the near neutral $u_* - V$ relationship would be adjusted to the smaller C_{dn} as the sloping terrain covered with corn stubble has z_0 smaller than the z_0 associated with the tree patch. That is, the u_* increase with V would be reduced to the value similar to the one from the reference wind sector.

The above analyses indicate that with the addition of the upslope tree patch for enhancing vertical transport of the cold surface air, the downstream increasing stable stratification with height is effectively reduced by the elevated cold air. The reduced stable stratification can assist bulk shear for its efficient generation of the most energetic large turbulent eddies, resulting in the enhanced u_* for a given V. Therefore, the observed deviation of the near-neutral $u_* - V$ relationship from the upslope tree patch in Figure 6 is contributed by both upwind terrain slope and the upslope tree patch not for its enhance of turbulence intensity itself but for its dynamic impact on the downstream stratification.

3.2.2. SCP

We then investigate the contribution of the structures of four ranch buildings and a field supporting trailer located on the north plateau to the near neutral $u_* - V$ relationship measured at the main tower in the shallow valley about 16 m below during SGP (Figure 7a). We find a similar signature of the upslope large surface roughness on

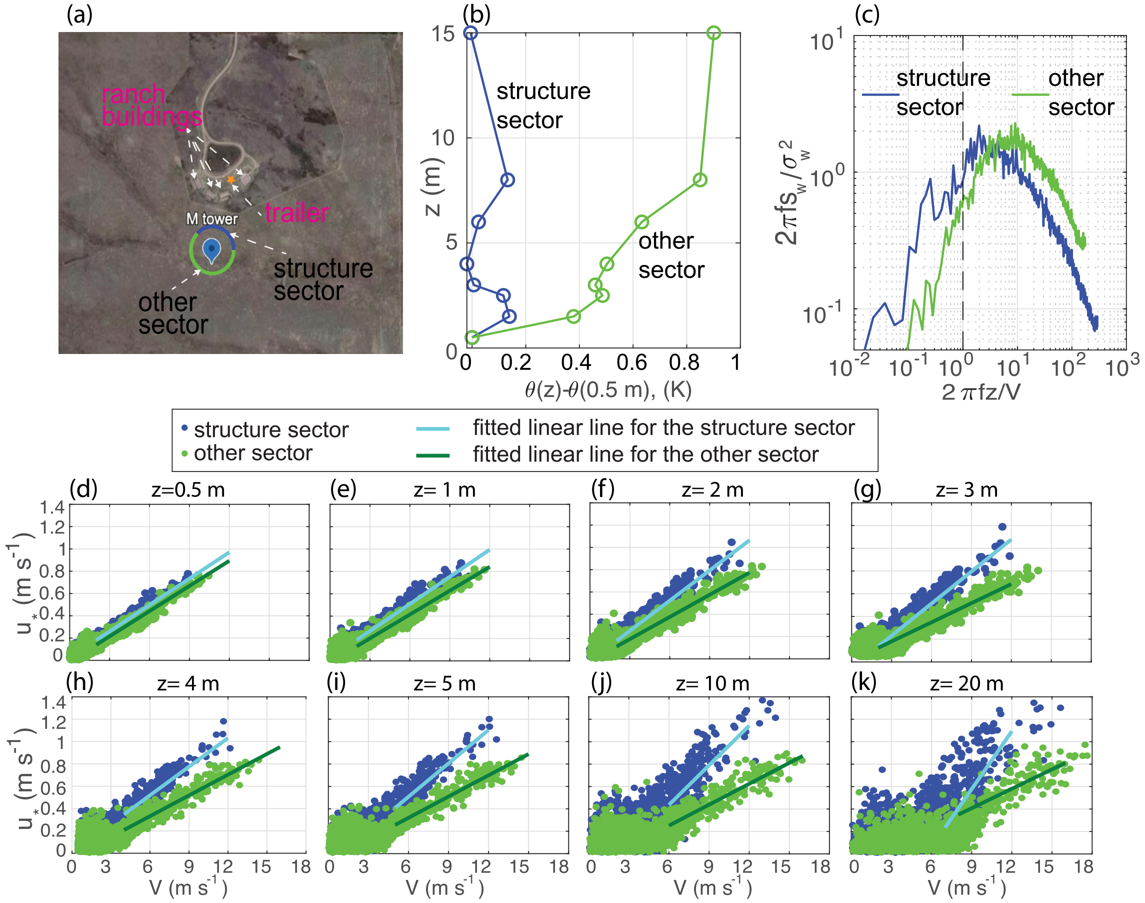

Figure 7. The observed $u_* - V$ relationships (d–k) at the labeled observation heights on the main tower (marked as M tower in a) during SCP for wind from the upslope structures of four ranch buildings and the trailer–the structure sector (marked in blue north of the M tower in a) and from the rest of wind directions (marked in green south of the M tower in a). The colors of the dots in (d–k) correspond to the colors of wind sectors in the areal satellite image (a). Similar to Figure 6, the potential temperature profiles relative to their surface values at 0.5 m averaged over all the clear nights for wind from the upslope structure direction and the other direction with $V > 6$ m s^{-1} at 20 m are shown in (b); the normalized w spectrum $2\pi f S_w \sigma_w^2$ as a function of the normalized frequency, $2\pi f z/V$ from both wind sectors are shown in (c). To ensure the spectral comparison is under near neutral conditions, the sonic anemometer measurements at $z = 20$ m between 0400 and 0600 LST on 10 October for $V \sim 7$ m s^{-1} from the other sector (green) and on 25 October for $V \sim 4$ m s^{-1} from the structure sector (blue) are used for the spectral analyses in (c). The cyan and dark green lines in (d–k) are the fitted linear lines for the structure and other sectors, respectively.

the downslope $u_* - V$ relationship as observed in Figure 6. The near-neutral $u_* - V$ linear relationship at 0.5 m in Figure 7d is approximately independent of wind direction, which further confirms the strong influence of the local surface to the $u_* - V$ relationship near the surface. The u_* increase with V is enhanced gradually with height for wind from the direction of the structures on the plateau–the structure sector of upwind direction of 320° to 90° instead of being invariant such as for wind from the other sector (Figure 7a).

Examination of the stratification and the normalized S_w from the two wind sectors also shows similar patterns as in Figure 6h. The stable stratification based on the sector-averaged temperature profiles is significantly weaker for wind from the structure sector than the one from the other sector especially at the upper tower levels (Figure 7b). And its normalized S_w peak at 20 m is also shifted toward the normalized low frequency in comparison with the one from the other sector under near-neutral conditions (Figure 7c). Considering the 20-m w power spectrum for a stronger wind, $V \sim 7$ m s^{-1} from the other sector than $V \sim 4$ m s^{-1} from the structure sector used in Figure 7c, the larger scale of the most energetic turbulent eddies from the structure sector further confirms the contribution of the reduction of the stable stratification by the upslope large surface roughness to the effective enhancement of the bulk-shear generated turbulence downstream. Although the distance of ~200 m between the upslope structures and the main tower is shorter than the distance of ~500 m between the upslope tree patch and the rel tower, the significant contribution of the bulk-shear generated turbulence to u_* as demonstrated in the spectral analysis indicates that the contribution of the advection of the enhanced turbulence from the structures to the observed u_* at the main tower is negligibly small.

Because of the significant terrain slope of $\gamma \approx 5°$ from the north plateau to the valley below, the enhanced u_* from the structure sector is visibly large such as at 10 and 20 m for $V = V_s \approx 6$ m s^{-1} in comparison with the one from the other sector due to the enhancement of hydrostatic imbalance related to the terrain slope for the increasing $\overline{w'^2}$ with height. Again, both upstream terrain elevation increase and the upslope structures contribute to the observed deviation of the near-neutral $u_* - V$ relationship from its relationship over the relatively flat surface around in Figures 7d–7k.

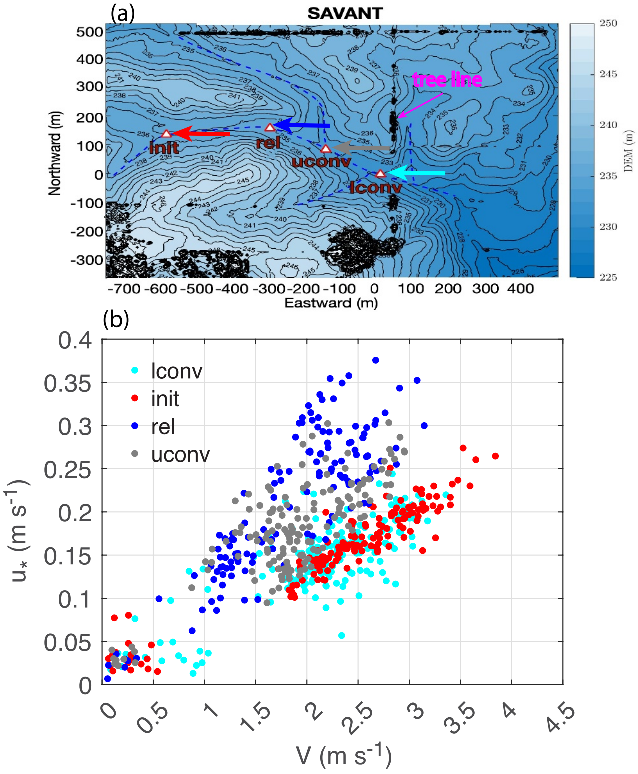

Figure 8. The 5-min $u_* - V$ relationships observed at 3-m above the surface on the four towers (b) for wind direction (WD) from east, $67.5° < WD < 112.5°$, marked with four vectors in (a). The observations from each tower in (b) have the same color as the wind vector at each tower in (a).

3.2.3. Different Impacts of Upwind Terrain With and Without Large Surface Roughness on the Downstream HOST Relationship

Over a flat surface, the growth of the most energetic turbulent eddies at a given z in the SBL is limited by the stable stratification and the bulk shear V/z. Because the required mechanical force for generating powerful large turbulent eddies to transport cold air up and warm air downward increases with height, the stable stratification as a result of bulk-shear generated turbulent mixing increases with height even when wind exceeds its threshold value at a given height. That is, the air is better mixed near the surface than above; the vertical mixing decreases with height. The increasing stable stratification with height is evident in the vertical temperature profile from the reference wind sector in Figure 6g as well as in the increasing standard deviation of u_* with height in the near-neutral $u_* - V$ line at all the towers in Figure 3. Under neutral conditions, turbulence intensity for a given bulk shear depends on surface roughness.

The analyses of the observations in Sections 3.1 and 3.2 indicate that upwind terrain slope alone and upward terrain slope with large surface roughness elements impact the downstream $u_* - V$ relationship differently mainly due to the contribution of the large surface roughness to the effective reduction of the downstream stable stratification. As the u_* increase with V is related to the neutral surface drag coefficient, which is uniquely controlled by the surface roughness under near neutral conditions, the u_* increase with V for downslope wind from uniform terrain is not impacted with the upstream terrain slope variation. For wind from elevated terrain with upslope large surface roughness, the spatial variation of turbulent mixing with the same bulk shear under neutral conditions would be significantly different. With the reduced surface roughness downstream from the upslope large surface roughness, bulk-shear-generated turbulent mixing would be reduced resulting in the somewhat decoupled vertical mixing downstream. Therefore, the downstream stratification as one of the two important factors in determining the HOST pattern is strongly impacted by the upstream elevated cold surface air from the enhanced turbulent mixing by the upslope large surface roughness. In other words, the downstream air temperature reduction as a result of horizontal transfer of upslope cold surface air is related to upwind terrain elevation. Without the vertical transport of the cold surface air by enhanced turbulent mixing, the downstream stable stratification cannot be effectively reduced. The stratification is critical for the generation of turbulence by bulk shear and a key factor for determining the near-neutral $u_* - V$ relationship.

3.3. Impacts of Shallow Complex Terrain on Turbulence Variation

The knowledge gained from Sections 3.1 and 3.2 helps us better understand the impact of shallow complex terrain on turbulence variation, such as the $u_* - V$ relationship at 3 m for the east wind sector between 67.5° and 112.5° from the four towers (Figure 8). We can see whether the observed HOST patterns in Figure 8b are related to terrain elevation change and surface-roughness variation within about 300 m from each tower as the influence of terrain features on the downstream $u_* - V$ relationship tends to decrease with distance.

The terrain for the upstream east wind sector varies significantly from grass in the main gully to the post-harvested soybean field and the windbreaker tree line on a north–south oriented ridge north of the main gully. The $u_* - V$ relationship at each of the four towers is impacted by its upstream terrain slope. The significant large surface roughness of the windbreaker tree line is only directly upstream of the rel and the uconc towers (Figure 8a). Because the easterly wind upstream of the init tower (marked with the red arrow in Figure 8a) is mainly from the short-grass-covered main gully with negligible terrain variation, its $u_* - V$ line has the narrowest spread among the four in Figure 8b and the lowest u_* for a given V. With the impact of the grass-covered main gully on the south and the post-harvested soybean on the north terrain above the main gully upstream of the lconv tower (from the direction of the cyan arrow in Figure 8a), the observation points are scattered around its $u_* - V$ line. Due to the significant impact of the tree line on the rel and the uconv towers, their observation spread around their $u_* - V$ lines is much wider than the one at the init tower. Among the four towers, the ridge impacts the rel tower the most; thus, its $u_* - V$ line has the highest averaged u_* for a given V in Figure 8b. Figure 8b shows that in general, the near-neutral $u_* - V$ relationship from the four towers systematically shifts toward the increasing u_* with increasing upwind terrain slope as discussed in Section 3.1. Similar $u_* - V$ analysis could contribute to understand the spatial variation of wind and vertical temperature gradient on the area-averaged turbulent heat transfer over the SCP shadow complex terrain demonstrated in Mahrt et al. (2021).

4. Summary and Conclusions

Using the HOST $u_* - V$ relationship over flat terrain for its capture of the critical contribution of bulk shear to turbulence generation and subsequent stratification reduction in the SBL, we investigate the impact of shallow complex terrain on turbulence generation in the clear-night SBL. We identify that an increase in upwind terrain slope, with and without upslope large surface roughness elements, affects downstream stable stratification differently, resulting in the observed different u_* increase with V. The impact of these terrain features on the downstream near-neutral $u_* - V$ relationship can be distinctly observed in the deviations of the near-neutral $u_* - V$ relationship from the reference HOST relationship over flat terrain as schematically summarized in Figure 9.

By comparing the near-neutral $u_* - V$ relationships for wind from different terrain slopes with the same surface roughness, we find downslope airflow reduces the downstream air temperature but has minimal impact on the stratification. This is because air temperature in the clear SBL is uniquely controlled by the bulk-shear (V/z) generated large eddy mixing of the increasing warm air with height, airflow coming down from high terrain entrains cold surface air along the slope, resulting in an increasingly deeper and colder air layer downstream. The cold downslope wind is observed to contribute to the enhancement of hydrostatic imbalance $-(\partial \overline{p}/\partial z + \overline{\rho} g)$ responsible for the enhancement of the vertical increase of vertical velocity variance $\overline{w'^2}$ from its zero surface value. As u_* is directly related to $\overline{w'^2}$ for a given bulk shear V/z, the resulting $u_* - V$ relationship shifts toward an increasing u_* with terrain slope (represented by the blue near-neutral linear $u_* - V$ line in Figure 9a, corresponding to the blue temperature profile in Figure 9b). However, the upstream terrain slope variation does not impact the rate of the u_* increase with V in the near-neutral $u_* - V$ line, which is determined by the neutral surface drag coefficient related to terrain surface roughness.

Examining the near-neutral $u_* - V$ relationships for wind from upslope large surface roughness elements, such as trees and buildings, we find that the near-neutral u_* increase with V is enhanced with height as illustrated in Figure 9a. Besides the contribution of the terrain slope to u_* enhancement, large surface roughness enhances turbulent mixing, which allows the elevated cold upstream air to replace the upper warm air in the downstream SBL as illustrated in Figure 6b. This reduction of the stable stratification with increasing height counteracts the normal increase in stable stratification with height in a typical near-neutral SBL (Figure 9b). With reduced stable stratification, the bulk shear V/z efficiently generates large turbulent eddies, leading to an increase in u_* for a given V. Between the upslope large surface roughness element and the downstream tower, both energy dissipation and airflow over the relatively small surface-roughness sloping terrain reduce the turbulence intensity initialy enhanced by the upslope roughness elements. Thus, the direct contribution of the enhanced turbulent mixing over upslope large surface roughness element to downstream u_* through advection does not fully explain the vertical increasing in u_* enhancement with V.

The study highlights the advantage of using the $u_* - V$ HOST relationship to understand key physical mechanisms influencing turbulence variation in shallow complex terrain in the nighttime SBL. Because turbulence

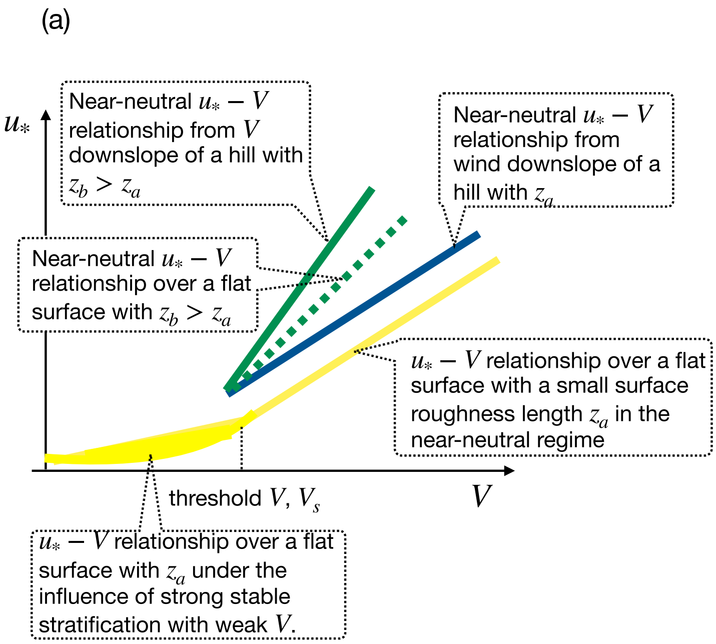

Figure 9. Schematic illustration of (a) the deviation of the observed HOST from the reference HOST over a flat terrain with z_a (yellow) due to an upstream terrain slope with a uniform surface roughness z_a (blue) and the upslope large surface roughness $z_b > z_a$ (solid green), and (b) the corresponding potential temperature profiles associated with the different terrain features in the same colors. The dashed green in (a) is the $u_* - V$ relationship over a flat surface with z_b.

intensity is determined directly by turbulence eddies generated by bulk-shear and indirectly by contribution of these eddies to reduction of the stable stratification through turbulent mixing over flat terrain in the SBL, physical processes affecting turbulence intensity can be identified through deviations of the observed $u_* - V$ relationship from the reference one over flat terrain. Further investigation of turbulence variation beyond shallow complex terrain is needed such as effects of large terrain elevation changes and radiation impacts of clouds and surrounding terrain on turbulence variation.

Acknowledgments

We would like to thank NSF/NCAR/EOL staff, especially Steve Oncley, William Brown, Edward Patton, and several students who participated in SAVANT and helped with analyzing the field data. We would also like to thank anonymous reviewers for their constructive comments. Funding for this study was supported by the U.S. National Science Foundation (NSF) awards: AGS-2203248, AGS-2220664, and AGS-2231229 for JS; AGS-1733877 and AGS-2220663 for JW, SB, and DK; AGS-1733746, AGS-1843258, and AGS-2220662 as well as the University of South Carolina Department of Geography for AH; AGS-2309208 for LM, and AGS-1844426 for GP. SB was also partly supported by the NOAA cooperative agreement NA220AR4320151 for the Cooperative Institute for Earth System Research and Data Science (CIESRDS). The statements, findings, conclusions, recommendations, and opinions expressed here are those of the authors and do not necessarily reflect the views of the NSF, NOAA, the U.S. Department of Commerce, the Illinois State Water Survey, the Prairie Research Institute, the University of Illinois, or the University of South Carolina.

Conflict of Interest

The authors declare no conflicts of interest relevant to this study.

Data Availability Statement

The SAVANT and the SCP field data sets used in this study are from NSF/UCAR/NCAR-Earth Observing Laboratory at https://doi.org/10.26023/NKWR-EYWS-5J0W and https://doi.org/10.5065/D6ZC8136, respectively. The high resolution DEM from the site survey is at https://doi.org/10.26023/9X98-348Q-V14. All are freely available to the public.

References

Acevedo, O. C., Costa, F. D., Maroneze, R., Carvalho, A. D., Puhales, F. E. S., & Oliveira, P. E. S. (2021). External controls on the transition between stable boundary-layer turbulence regimes. *Quarterly Journal of the Royal Meteorological Society*, *147*(737), 2335–2351. https://doi.org/10.1002/qj.4027

Acevedo, O. C., Mahrt, L., Puhales, F. S., Costa, F. D., Medeiros, L. E., & Degrazia, G. A. (2015). Contrasting structures between the decoupled and coupled states of the stable boundary layer. *Quarterly Journal of the Royal Meteorological Society*, *142*(695), 693–702. https://doi.org/10.1002/qj.2693

Andreas, E. L., Mahrt, L., & Vickers, D. (2012). A new drag relation for aerodynamically rough flow over the ocean. *Journal of the Atmospheric Sciences*, *69*(8), 2520–2537. https://doi.org/10.1175/jas-d-11-0312.1

Barbano, F., Brogno, L., Tampieri, F., & Di Sabatino, S. (2022). Interaction between waves and turbulence within the nocturnal boundary layer. *Boundary-Layer Meteorology*, *183*(1), 35–65. https://doi.org/10.1007/s10546-021-00678-2

Bhimireddy, S. R., Wang, J., Hiscox, A. L., & Kristovich, D. A. R. (2022). Influence of stability and surface roughness on turbulence during the Stable Atmospheric Variability and Transport (SAVANT) field campaign. *Journal of Applied Meteorology and Climatology*, *61*(9), 1273–1289. https://doi.org/10.1175/JAMC-D-21-0160.1

Bhimireddy, S. R., Sun, J., Wang, J., Kristovich, D. A. R., & Hiscox, A. L. (2024). Effect of small-scale topographical variations and fetch from roughness elements on the stable boundary layer turbulence statistics. *Boundary-Layer Meteorology*, *190*(3), 1–19. https://doi.org/10.1007/s10546-023-00855-5

Cava, D., Giostra, U., & Katul, G. (2015). Characteristics of gravity waves over an Antarctic ice sheet during an austral summer. *Atmosphere*, *6*(9), 1271–1289. https://doi.org/10.3390/atmos6091271

Cheng, X., Li, Q., Chen, H., Zheng, S., Chen, J., Zheng, H., et al. (2023). Multi-scale flow structure and its effect on momentum flux in the coastal marine atmospheric boundary layer. *Flow*, *3*, E29. https://doi.org/10.1017/flo.2023.24

Dias-Júnior, C. Q., Sá, L. D. A., Marques Filho, E. P., Santana, R. A., Mauder, M., & Manzi, A. O. (2017). Turbulence regimes in the stable boundary layer above and within the Amazon forest. *Agric. For. Meteorol.*, *233*, 122–132. https://doi.org/10.1016/j.agrformet.2016.11.001

Garratt, J. R. (1992). *The atmospheric boundary layer. Cambridge atmospheric and space science series*. Cambridge University Press.

Geiger, R., Aron, R. H., & Todhunter, P. (1995). *The climate near the ground* (5th ed.). Harvard University Press.

Grisogono, B., Sun, J., & Belušić, D. (2020). A note on MOST and HOST for turbulence parameterization. *Quarterly Journal of the Royal Meteorological Society*, *146*(729), 1991–1997. https://doi.org/10.1002/qj.3770

Hiscox, A., Bhimireddy, S., Wang, J., Kristovich, D. A. R., Sun, J., Patton, E. G., et al. (2023). Exploring influences of shallow topography in stable boundary layers: The SAVANT Field Campaign. *Bulletin America Meteorology Social*, *104*(2), E520–E541. https://doi.org/10.1175/bams-d-21-0332.1

Hoch, S. W., Whiteman, C. D., & Mayer, B. (2011). A systematic study of longwave radiative heating and cooling within valleys and basins using a three-dimensional radiative transfer model. *Journal of Applied Meteorology and Climatology*, *50*(12), 2473–2489. https://doi.org/10.1175/jamc-d-11-083.1

Huang, M., Gao, Z., Miao, S., Chen, F., LeMone, M. A., Li, J., et al. (2017). Estimate of boundary-layer depth over Beijing, China, using Doppler Lidar data during SURF-2015. *Boundary-Layer Meteorology*, *162*(3), 503–522. https://doi.org/10.1007/s10546-016-0205-2

Lan, C., Xie, J., Li, L., Wang, B., Yang, H., & Lu, J. (2023). Downward momentum flux: An important mechanism of typhoon maintaining ground destructive force. *Journal of Geophysical Research*, *128*(8), e2022JD037470. https://doi.org/10.1029/2022jd037470

Lehner, M., Whiteman, C. D., Hoch, S. W., Jensen, D., Pardyjak, E. R., Leo, L. S., et al. (2015). A case study of the nocturnal boundary layer evolution on a slope at the foot of a desert mountain. *Journal of Applied Meteorology and Climatology*, *54*(4), 732–751. https://doi.org/10.1175/jamc-d-14-0223.1

Liang, X., Miao, S., Li, J., Bornstein, R., Zhang, X., Gao, Y., et al. (2018). SURF: Understanding and predicting urban convection and haze. *Bulletin America Meteorology Social*, *99*(7), 1391–1413. https://doi.org/10.1175/BAMS-D-16-0178.1

Mahrt, L. (2017). Stably stratified flow in a shallow valley. *Boundary-Layer Meteorology*, *162*, 1–20. https://doi.org/10.1007/s10546-016-0191-4

Mahrt, L. (2022). Horizontal variations of nocturnal temperature and turbulence over microtopography. *Boundary-Layer Meteorology*, *184*(3), 401–422. https://doi.org/10.1007/s10546-022-00721-w

Mahrt, L., Belusic, D., & Acevedo, O. (2021). Small-scale spatial variation of the nocturnal wind field. *Boundary-Layer Meteorology*, *180*(2), 225–245. https://doi.org/10.1007/s10546-021-00627-z

Mahrt, L., & Heald, R. (2015). Common marginal cold pools. *Journal of Applied Meteorology and Climatology*, *54*(2), 339–351. https://doi.org/10.1175/jamc-d-14-0204.1

Mahrt, L., Sun, J., Oncley, S. P., & Horst, T. W. (2014). Transient cold air drainage down a shallow valley. *Journal of the Atmospheric Sciences*, *71*(7), 2534–2544. https://doi.org/10.1175/jas-d-14-0010.1

Mahrt, L., Sun, J., & Stauffer, D. (2015). Dependence of turbulent velocities on wind speed and stratification. *Boundary-Layer Meteorology*, *155*(1), 55–71. https://doi.org/10.1007/s10546-014-9992-5

Mahrt, L., Thomas, C., Richardson, S., Seaman, N., Stauffer, D., & Zeeman, M. (2013). Non-stationary generation of weak turbulence for very stable and weak-wind conditions. *Boundary-Layer Meteorology*, *147*(2), 179–199. https://doi.org/10.1007/s10546-012-9782-x

Mahrt, L., Thomas, C. K., Grachev, A. A., & Persson, P. O. G. (2018). Near-surface vertical flux divergence in the stable boundary layer. *Boundary-Layer Meteorology*, *169*(3), 373–393. https://doi.org/10.1007/s10546-018-0379-x

Maillard, J., Ravetta, F., Raut, J.-C., Fochesatto, G. J., & Law, K. S. (2022). Modulation of boundary-layer stability and the surface energy budget by a local flow in Central Alaska. *Boundary-Layer Meteorology*, *185*(3), 395–414. https://doi.org/10.1007/s10546-022-00737-2

Mazzola, M., Viola, A. P., Choi, T., & Tampieri, F. (2021). Characterization of turbulence in the neutral and stable surface layer at Jang Bogo Station, Antarctica. *Atmosphere*, *12*(9), 1095. https://doi.org/10.3390/atmos12091095

Medeiros, L. E., & Fitzjarrald, D. R. (2015). Stable boundary layer in complex terrain. Part II: Geometrical and sheltering effects on mixing. *Journal of Applied Meteorology and Climatology*, *54*(1), 170–188. https://doi.org/10.1175/jamc-d-13-0346.1

Mendonça, A. C., Dias-Júnior, C. Q., Acevedo, O. C., Santana, R. A., Costa, F. D., Negrón-Juarez, R. I., et al. (2023). Turbulence regimes in the nocturnal roughness sublayer: Interaction with deep convection and tree mortality in the Amazon. *Agric. For. Meteor.*, *339*, 109526. https://doi.org/10.1016/j.agrformet.2023.109526

Mortarini, L., Cava, D., Giostra, U., Acevedo, O., Nogueira Martins, L., Soares de Oliveira, P., & Anfossi, D. (2018). Observations of Submeso motions and intermittent turbulent mixing across a low level jet with a 132-m tower. *Quarterly Journal of the Royal Meteorological Society*, *144*(710), 172–183. https://doi.org/10.1002/qj.3192

NCAR/EOL In-situ Sensing Facility. (2021). NCAR/EOL ISFS Surface Meteorology and Flux Products, 5-minute, geographic coordinate and tilt corrected winds. (Version 2.0) [Dataset]. *UCAR/NCAR—Earth Observing Laboratory*. https://doi.org/10.26023/NKWR-EYWS-5J0W. Accessed 14 March 2023.

Noad, N. C., & Bonnaventure, P. P. (2024). Examining the influence of microclimate conditions on the breakup of surface-based temperature inversions in two proximal but dissimilar Yukon valleys. *Canadian Geographies/Géographies Canadiennes*, *68*(3), 323–339. https://doi.org/10.1111/cag.12886

Peltola, O., Lapo, K., & Thomas, C. K. (2021). A physics-based universal indicator for vertical decoupling and mixing across canopies architectures and dynamic stabilities. *Geophysical Research Letters*, *48*(5), e2020GL091615. https://doi.org/10.1029/2020gl091615

Petty, G. (2019). SAVANT field site Orthophoto and high resolution DEM. (Version 1.0) [Dataset]. *UCAR/NCAR—Earth Observing Laboratory*. https://doi.org/10.26023/9X98-348Q-V14. Accessed 20 Mar 2024.

Pfister, L., Lapo, K., Sayde, C., Selker, J., Mahrt, L., & Thomas, C. K. (2019). Classifying the nocturnal atmospheric boundary layer into temperature and flow regimes. *Quarterly Journal of the Royal Meteorological Society*, *145*(721), 1515–1534. https://doi.org/10.1002/qj.3508

Román-Cascón, C., Yagüe, C., Mahrt, L., Sastre, M., Steeneveld, G.-J., Pardyjak, E., et al. (2015). Interactions among drainage flows, gravity waves and turbulence: A BLLAST case study. *Atmospheric Chemistry and Physics*, *15*(15), 9031–9047. https://doi.org/10.5194/acp-15-9031-2015

Russell, E. S., Liu, H., Gao, Z., Lamb, B., & Wagenbrenner, N. (2016). Turbulence dependence on winds and stability in a weak-wind canopy sublayer over complex terrain. *Journal of Geophysical Research*, *121*(19), 11502–11515. https://doi.org/10.1002/2016jd025057

Shao, X., Zhang, N., Li, D., & Sun, J. (2023). A non-dimensional index for characterizing the transition of turbulence regimes in stable atmospheric boundary layers. *Geophysical Research Letters*, *50*(18), e2023GL105304. https://doi.org/10.1029/2023gl105304

Stull, R. B. (1988). *An introduction to boundary layer meteorology*. Kluwer Academic Publishers.

Sun, J., & French, J. R. (2016). Air-sea interaction in light of new understanding of air-land interactions. *Journal of the Atmospheric Sciences*, *73*(10), 3931–3949. https://doi.org/10.1175/JAS-D-15-0354.1

Sun, J., Lenschow, D. H., LeMone, M. A., & Mahrt, L. (2016). The role of large-coherent-eddy transport in the atmospheric surface layer based on CASES-99 observations. *Boundary-Layer Meteorology*, *160*(1), 83–111. https://doi.org/10.1007/s10546-016-0134-0

Sun, J., Mahrt, L., Banta, R. M., & Pichugina, Y. L. (2012). Turbulence regimes and turbulence intermittency in the stable boundary layer during CASES-99. *Journal of the Atmospheric Sciences*, *69*(1), 338–351. https://doi.org/10.1175/jas-d-11-082.1

Sun, J., Mahrt, L., Nappo, C., & Lenschow, D. H. (2015). Wind and temperature oscillations generated by wave-turbulence interactions in the stably stratified boundary layer. *Journal of the Atmospheric Sciences*, *72*(4), 1484–1503. https://doi.org/10.1175/JAS-D-14-0129.1

Sun, J., Nappo, C. J., Mahrt, L., Belušić, D., Grisogono, B., Stauffer, D. R., et al. (2015). Review of wave-turbulence interactions in stable atmospheric boundary layer. *Review of Geophysics*, *53*(3), 956–993. https://doi.org/10.1002/2015RG000487

Sun, J., Takle, E. S., & Acevedo, O. C. (2020). Understanding physical processes represented by the Monin–Obukhov bulk formula for momentum transfer. *Boundary-Layer Meteorology*, *177*(1), 69–95. https://doi.org/10.1007/s10546-020-00546-5

Sun, J., Wulfmeyer, V., Späth, F., Vömel, H., Brown, W., & Oncley, S. (2024). Investigation of hydrostatic imbalance with field observations. *Journal of Applied Meteorology and Climatology*, *63*(1), 3–25. https://doi.org/10.1175/jamc-d-22-0206.1

UCAR/NCAR—Earth Observing Laboratory. (2014). SCP 5 minute ISFS data, QC'd, geographic and tilt corrected sonic winds. (Version 1.0) [Dataset]. *UCAR/NCAR—Earth Observing Laboratory*. https://doi.org/10.5065/D6ZC8136. Accessed 23 March 2023.

van de Wiel, B. J. H., Moene, A. F., Jonker, H. J. J., Baas, P., Basu, S., Donda, J. M. M., et al. (2012). The minimum wind speed for sustainable turbulence in the nocturnal boundary layer. *Journal of the Atmospheric Sciences*, *69*, 3116–3127. https://doi.org/10.1175/JAS-D-12-0107.1

Vignon, E., van de Wiel, B. J. H., van Hooijdonk, I. G. S., Genthon, C., van der Linden, S. J. A., van Hooft, J. A., et al. (2017). Stable boundary-layer regimes at dome c, Antarctica: Observation and analysis. *Quarterly Journal of the Royal Meteorological Society*, *143*(704), 1241–1253. https://doi.org/10.1002/qj.2998

Wang, X.-C., Liu, F., & Wang, C.-K. (2022). Radiation and energy balance on a hillslope forest: Horizontal versus slope-parallel installation of radiometer. *Journal Mountain Science- Engl*, *19*(11), 3076–3087. https://doi.org/10.1007/s11629-022-7481-8

Wyngaard, J. C. (2010). *Turbulence in the Atmosphere*. Cambridge University Press.